Back to Session Subjects

Application of the Finite State Unsteady Wake Model in Helicopter Flight Dynamic Simulation

Mario Hamers
Deutsches Zentrum für Luft- und Raumfahrt e.V. (DLR)
Institute of Flight Research
Braunschweig, Germany

Pierre-Marie Basset
Office Nationale d'Etudes et de Recherches Aérospatiales (ONERA)
System Control and Flight Dynamics Department
Salon de Provence, France

Abstract

The Finite State Unsteady Wake Model as presented by He and Peters showed to be an accurate and powerful formulation in order to calculate the dynamic rotor induced inflow distribution. The complexity of the model and therewith the local resolution over the rotor disk can easily be adapted to the specific user application. This makes it well suited for use in sophisticated dynamic helicopter simulations. DLR and ONERA have implemented the model in their respective simulation codes. The application at ONERA concentrates mainly on aspects concerning the interaction of the wake with other components, whereas at DLR the realtime application in the ACT/FHS system simulator is of major interest.

This paper will highlight the application of this model in both non-linear off-line and realtime helicopter simulation. The advantages, disadvantages and the range of application will be discussed. Also, comparison with other theories and validation calculations using flight test data are performed.

Notations

$e_i = (x, y, z)^T$	coordinate frame components, [-]
$\hat{e}_i = (\hat{x}, \hat{y}, \hat{z})^T$	ground frame components, [-]
$e_{i\xi} = (x_\xi, y_\xi, z_\xi)^T$	freestream frame components, [-]
m, r, l	harmonic number, [-]
$n,\ j, k$	shape number, [-]
p	non dimensional pressure, [-]
p_{TPP}, q_{TPP}	tip path plane motion, [rad/s]
r	non dimensional rotor radius, [-]
t	non dimensional time, [-]
v	geometric influence coefficients, [-]
$v_i = (u, v, w)^T$	inflow velocity components, [-]
$v_{i\xi} = (u_\xi, v_\xi, w_\xi)^T$	freestream inflow components, [-]
C, D	influence matrices for ground effect, [-]
$F_{b,e}$	blade element lift force, [N]
G	resulting gain matrix for ground effect, [-]
H	Legendre derivative function matrix, [-]
H_{alt}	altitude above ground, [-]
K_p, K_q	wake distortion coefficients, [-]
L	inflow gain matrices, [-]
M	mass matrix, [-]
N_b	number of blades, [-]
N_e	number of blade elements, [-]
$\bar{P}, \bar{Q}$	normalized associated Legendre functions of first and second kind, [-]
R	rotor radius, [m]
V	flow matrix, [-]
V_M	non dimensional flow parameter, [-]
V_T	total flow parameter, [-]
V_∞	free stream velocity, [-]
α, β	induced inflow coefficients, [-]
χ	wake skew angle, [rad]
δ	switch function, [-]
δ_{ij}	Kronecker symbol, [-]
$\lambda, \lambda_f, \lambda_m$	inflow parameters, [-]
μ	disk advance ratio, [-]
ν, η, ψ	ellipsoidal coordinates, [-]
$\hat{\nu}, \hat{\eta}, \hat{\psi}$	ellipsoidal coordinates in ground frame, [-]
ρ	air density, [kg/m^3]
σ	ground effect coefficients, [-]
τ	pressure coefficients (generalized forces), [-]
ξ	freestream coordinate, [-]
ψ_b	blade azimuth, [rad]
ψ_B	helicopter heading, [rad]

Presented at the 26th European Rotorcraft Forum, 26-29 September 2000, Netherlands Congress Centre, The Hague, The Netherlands

ψ_{wa} wind axis direction, [rad]
Φ non dimensional pressure potential, [-]
Γ wake integral functions, [-]
Ω rotor speed, [rad/s]
Ψ radial shape function, [-]

$(\ )_{,t} = \overset{*}{(\ )}$ differentiation w.r.t. non dimensional time
$(\ )_{,i}$ differentiation along i[th] coordinate direction
$(\ )_{,\xi}$ differentiation along freestream line

Introduction

In the field of rotorcraft research, both at ONERA and DLR, helicopter flight dynamic modeling is a major issue. A wide range of applications, e.g. rotor aerodynamic and aeroelastic studies, helicopter performance and stability investigations, realtime and pilot-in-the-loop simulations for handling qualities investigations, require accurate consistent mathematical helicopter models. In recent years, a lot of effort has been made to improve the prediction capability and accuracy of helicopter dynamic simulation tools with special emphasis on the prediction of helicopter cross coupling behavior excited by pilot cyclic control inputs. In this context, one of the approaches investigated and implemented is the dynamic inflow model of Pitt and Peters [1], describing the 3 state rotor inflow distribution by a set of ordinary differential equations governed by the global aerodynamic thrust as well as roll and pitch moments. As shown in several publications (e.g. [2], [3], [4]) this model allows an improvement in on-axis as well as off-axis predicted dynamic helicopter responses.

However, this model is a low order approximation to the rotor induced flow field and hence is inadequate to describe the more complex flow field distributions (e.g. non linear radial inflow distribution). In forward flight the non-uniform flow distribution is known to be important to correctly predict the helicopter dynamics. Also higher harmonic components in the rotor wake are known to have an influence on helicopter trim and dynamic simulation. Further, for investigations of interactions between main rotor wake and fuselage or tail components, a dynamic inflow model is required which provides induced velocity not only at the rotor disk itself but also at an arbitrary point outside the disk. A promising approach which incorporates Pitt&Peters theory but beyond that overcomes above disadvantages was found in the *Finite State Unsteady Wake Model* [5], [6]. In this formulation presented by He and Peters, the inflow is expanded in terms of higher harmonic functions for azimuthal distribution and radial shape functions using Legendre polynomial functions. The resulting set of equations governing the dynamic inflow states are driven by the present (arbitrary) blade lift distribution. A major advantage is that the number of harmonic and shape functions and thus the number of coefficients can be defined by the user in dependence of the particular application which makes the model well suited for a wide range of different investigations. Especially the use of this formulation in combination with a modal blade dynamic approach guarantees a balance between the complexity of dynamic and aerodynamic modeling.

The Finite State Unsteady Wake model is already implemented in comprehensive simulation programs as FlightLab [7]. Numerous papers show the power, the wide range of application and the constant contribution of new model extensions [8], [9], [10], [11].

Within the close cooperation between DLR and ONERA and in the scope of a personnel exchange, it was decided to study the Finite State Unsteady Wake Model and make it available for both offline and realtime simulations operated at DLR and ONERA. This is done by implementing the model in the common ONERA/DLR helicopter simulation environment HOST (Helicopter Overall Simulation Tool, developed by Eurocopter [12]) and in the new system simulator environment for the ACT/FHS flying helicopter simulator [13], a pure realtime application at DLR.

General theory

Pressure potential

Since the theoretical background of the Finite State Unsteady Wake Model is explained extensively in literature [5], [6], [14], [15], here only a brief description of the principal theory will be given. Similar to the Pitt&Peters formulation the Finite State Unsteady Wake Model bases on a pressure perturbation function Φ, describing an acceleration potential in an incompressible potential flow field. Considering the principal fluid mechanic equations for conservation of mass and momentum in dimensionless notation:

$$v_{i,i} = 0 \tag{1}$$

$$v_{i,t} - V_\infty \cdot v_{i,\xi} = -\Phi_{,i} \tag{2}$$

a division of the pressure function in a convection part Φ^V and an acceleration part Φ^A seems reasonable:

$$\Phi = \Phi^V + \Phi^A \tag{3}$$

with:

$$\Phi^V_{,i} = V_\infty \cdot v_{i,\xi} \quad , \quad \Phi^A_{,i} = -v_{i,t} \tag{4}$$

The convection part describes the pressure variation along the flow line, whereas the acceleration or unsteady part counts for the variation with time. Differentiating equation (4) shows that both pressure function parts satisfy Laplace's equation:

$$\Phi^{V}_{,ii} = 0 \quad , \quad \Phi^{A}_{,ii} = 0 \tag{5}$$

Kinner was the first to show that an analytical solution for the pressure function can be obtained for a circular wing or a disk, when expressing the Laplace equations in ellipsoidal coordinates and expanding with Legendre polynomial functions [16]. For zero pressure perturbation at infinity the overall pressure function becomes:

$$\Phi = -\frac{1}{2}\sum_{m=0}^{\infty}\sum_{\substack{n=m+1,\\ m+3,..}}^{\infty} \bar{P}_n^m(\nu)\cdot\bar{Q}_n^m(i\eta)\cdot \cdot\left(\tau_n^{mc}(\bar{t})\cos m\psi + \tau_n^{ms}(\bar{t})\sin m\psi\right) \tag{6}$$

where ν, η, ψ are ellipsoidal coordinates (see appendix) and $\bar{P}_n^m$ and $\bar{Q}_n^m$ are the normalized associated Legendre functions of the first and second kind. The arbitrary cosine and sine coefficients τ_n^{mc} and τ_n^{ms} are functions of the present disk loads and thus vary with time. The index *m* denotes the respective harmonic number and *n* the mode shape related to harmonic *m*. The Legendre functions are defined only for $n \geq m$.

Equation (6) describes an arbitrary pressure distribution field from a circular disk with a pressure discontinuity across the disk itself. The resulting lifting pressure distribution, i.e. the difference between the upper and lower surface pressure, matching the present disk loads can then be written as:

$$p = -2\cdot\Phi(\nu, \eta = 0, \psi) \tag{7}$$

The advantage of the formulation in (6) is that through the double summation the individual terms can be treated separately, since orthogonality is obtained in azimuthal as well as radial direction. The Fourier terms $\cos m\psi$ and $\sin m\psi$ guarantee orthogonality in azimuth, whereas the Legendre radial shape functions are generally linear independent and thus satisfy:

$$\int_{-1}^{1} \bar{P}_n^m(\nu)\cdot\bar{P}_{n'}^m(\nu)\,d\nu = 2\,\delta_{nn'} \tag{8}$$

with the Kronecker symbol $\delta_{nn'} = 1$ for $n = n'$ and $\delta_{nn'} = 0$ for $n \neq n'$. For a given harmonic *m* all shapes *n* are thus orthogonal. In rotor application, however, only a definition of the shape functions from rotor hub to blade tip is of interest, thus changing the integration boundaries. In this case orthogonality is only given for $m+n = odd$:

$$\int_{0}^{1} \bar{P}_n^m(\nu)\cdot\bar{P}_{n'}^m(\nu)\,d\nu = \delta_{nn'} \quad , \quad m+n = odd \tag{9}$$

a condition which is reflected in the running index of the second sum in equation (6): $n = m+1, m+3, \ldots$

Since pressure function at the left hand sides of equation (4) is expressed in terms of Fourier and Legendre functions, a more or less similar expansion for the induced velocity at the right hand side makes sense. For the moment, only the induced velocities at the rotor disk ($\eta = 0$) are of interest. The normal component of the induced velocity w ($= v_z$) at the disk can then be expressed as:

$$w = \sum_{r=0}^{\infty}\sum_{\substack{j=r+1,\\ r+3,..}}^{\infty} \Psi_j^r(\nu)\cdot\left(\alpha_j^r(t)\cos r\psi + \beta_j^r(t)\sin r\psi\right) \tag{10}$$

where α_j^r and β_j^r are the inflow states with respect to shape function Ψ_j^r.

For solving the unsteady part Φ^A of the pressure function, it appeared that using:

$$\Psi_j^r = \frac{\bar{P}_j^r(\nu)}{\nu} \tag{11}$$

for the shape function in (10) achieves a good convergence of the model. An analytical expansion of this Ψ_j^r is shown in the appendix. From (4), we obtain for the induced velocity acceleration at the rotor disk ($\eta = 0$):

$$w_{,t} = \overset{*}{w} = -\left.\frac{\partial\Phi^A}{\partial z}\right|_{\eta=0} \tag{12}$$

Substituting the pressure and velocity functions and making a comparison of coefficients leads to:

$$\overset{*}{\alpha}_j^r = -\frac{1}{2}\tau_n^{mc}\cdot\left.\frac{\partial\bar{Q}_n^m(i\eta)}{\partial\eta}\right|_{\eta=0} = \tau_n^{mc}\cdot\frac{\pi}{4H_n^m} \tag{13}$$

$$\overset{*}{\beta}_j^r = -\frac{1}{2}\tau_n^{ms}\cdot\left.\frac{\partial\bar{Q}_n^m(i\eta)}{\partial\eta}\right|_{\eta=0} = \tau_n^{ms}\cdot\frac{\pi}{4H_n^m} \tag{14}$$

where H_n^m is used to substitute the Legendre function derivatives. An analytical expression of H_n^m is given in the appendix.

For calculating the steady induced velocity at the rotor disk, the convection part of the pressure potential Φ^V has to be integrated along a freestream flow line from rotor disk to infinity:

$$w = -\frac{1}{V_\infty}\int_0^\infty \frac{\partial \Phi^V}{\partial z} d\xi \tag{15}$$

Here, the velocity radial shape function from (10) is assumed as:

$$\Psi_j^r = \bar{P}_j^r(\nu) \tag{16}$$

Substituting velocity and pressure functions leads to:

$$\hat{\alpha}_j^r = V^{-1} \cdot \hat{L}_{jn}^{rmc} \cdot \frac{1}{2}\tau_n^{mc} \tag{17}$$

$$\hat{\beta}_j^r = V^{-1} \cdot \hat{L}_{jn}^{rms} \cdot \frac{1}{2}\tau_n^{ms} \tag{18}$$

where $\hat{L}_{jn}^{rms}$ and $\hat{L}_{jn}^{rms}$ are the gain matrices having elements which are integral functions of the form:

$$\hat{L}_{jn}^{rmc} = \frac{1}{\delta\pi}\int_0^{2\pi}\int_0^1 \bar{P}_j^r(\nu_0)\cos r\psi \int_0^\infty \frac{\partial}{\partial z}\left(\bar{P}_n^m(\nu)\bar{Q}_n^m(i\eta)\right)\cdot \cdot\cos m\psi \, d\xi d\nu d\psi \tag{19}$$

$$\hat{L}_{jn}^{rms} = \frac{1}{\pi}\int_0^{2\pi}\int_0^1 \bar{P}_j^r(\nu_0)\sin r\psi \int_0^\infty \frac{\partial}{\partial z}\left(\bar{P}_n^m(\nu)\bar{Q}_n^m(i\eta)\right)\cdot \cdot\sin m\psi \, d\xi d\nu d\psi \tag{20}$$

with $\delta = 2$ for $r = 0$ and $\delta = 1$ for $r \neq 0$. The hat in equations (17) and (18) indicates, that in order to derive the inflow states another velocity shape function is assumed. V is a diagonal matrix consisting of the free stream velocity V_∞ in the main diagonal.

Combining equations (13), (14) and (17), (18) gives:

$$M \cdot \overset{*}{\alpha}_j^r + \left(\hat{L}_{jn}^{rmc}\right)^{-1} \cdot V \cdot \hat{\alpha}_j^r = \frac{1}{2}\tau_n^{mc} \tag{21}$$

$$M \cdot \overset{*}{\beta}_j^r + \left(\hat{L}_{jn}^{rms}\right)^{-1} \cdot V \cdot \hat{\beta}_j^r = \frac{1}{2}\tau_n^{ms} \tag{22}$$

with a mass matrix: $M = 2H_n^m/\pi$ (23)

To overcome the difference in the shape function assumption from (11) and (16) the $\hat{L}$ matrix has to be corrected. Additionally, the obtained $\bar{L}$ matrix and the flow states and pressure coefficients are normalized with $2\sqrt{H_n^m/\pi}$ (indicated with an additional bar). The resulting linear equation system can then be written as:

$$\left(\bar{\bar{L}}_{jn}^{rmc}\right)\cdot \overset{*}{\bar{\alpha}}_j^r = -V_n^m \cdot \bar{\alpha}_j^r + \left(\bar{\bar{L}}_{jn}^{rmc}\right)\cdot \bar{\tau}_n^{mc} \tag{24}$$

$$\left(\bar{\bar{L}}_{jn}^{rms}\right)\cdot \overset{*}{\bar{\beta}}_j^r = -V_n^m \cdot \bar{\beta}_j^r + \left(\bar{\bar{L}}_{jn}^{rms}\right)\cdot \bar{\tau}_n^{ms} \tag{25}$$

The matrices $\bar{\bar{L}}$ consists of a time independent part Γ (which can be calculated in advance) and a time varying part depending on the present wake skew angle. In hover and axial flight, $\bar{\bar{L}}$ are matrices with diagonal character. In forward flight, numerous elements are non zero and thus provide an "interstate" coupling between the individual inflow states. Analytical expressions for the matrices are given in the appendix

Inflow considerations

As a refinement of the theory, the diagonal mass flow matrix V_n^m is used instead of *V*. The new matrix consists of equivalent velocity: $V_1^0 = V_M$ and steady state velocity: $V_n^m = V_T$, $(m \neq 0, n \neq 1)$ elements on its main diagonal. The velocity parameters are derived as:

$$V_T = \sqrt{\mu^2 + \lambda^2} \tag{26}$$

$$V_M = V_T + \frac{\lambda\lambda_m}{V_T} \tag{27}$$

Here μ is the advance ratio and $\lambda = \lambda_f + \lambda_m$ the total inflow, which is the freestream inflow λ_f plus the induced mean inflow λ_m from momentum conservation,

with: $$\lambda_m = \frac{\sqrt{3\pi}}{2}\bar{\alpha}_1^0 \tag{28}$$

Further, the wake skew angle can be derived as:

$$\tan\chi = \frac{\mu}{\lambda} \tag{29}$$

The above set of equations allows an analytical calculation of the time-dependent induced velocity derivatives directly from an instantaneous pressure distribution on the rotor disk and in dependence of the present flow conditions. In each integration step, the derivatives are integrated by a numerical method to the actual inflow states. These are then used to calculate the flow distribution and subsequently the resulting blade loads.

Generalized forces

In order to calculate the pressure coefficients τ_n^m (i.e. the generalized forces) the theory includes an analytical transition for the governing equations from a continuous pressure distribution on a rotor disk to a load distribution on discrete rotor blades. A simplification can be made when instead of a blade spanwise pressure distribution a lifting line, or even blade element lift is assumed. Both helicopter simulation programs mentioned before use a blade element method to calculate the resulting blade element loads. Calculation of the pressure coefficients then becomes:

$$\bar{\tau}_n^{m\,c} = \frac{1}{\delta\pi}\sum_1^{N_b}\sum_1^{N_e}\frac{F_{b,e}}{\rho\Omega^2R^4}\cdot\frac{\bar{P}_n^m(\nu)}{\nu}\cdot\sqrt{\frac{\pi}{4H_n^m}}\cdot\cos m\psi_b \quad (30)$$

$$\bar{\tau}_n^{m\,s} = \frac{1}{\pi}\sum_1^{N_b}\sum_1^{N_e}\frac{F_{b,e}}{\rho\Omega^2R^4}\cdot\frac{\bar{P}_n^m(\nu)}{\nu}\cdot\sqrt{\frac{\pi}{4H_n^m}}\cdot\sin m\psi_b \quad (31)$$

where $F_{b,e}$ is the lift of the particular blade element.

Model limits

Although the model finds a broad application, it cannot cover all occurring physical phenomena with respect to rotor dynamics and aerodynamics. Besides the restrictions due to the incompressible flow assumption, the model does not represent effects due to blade vortices and blade vortex interactions and is, therefore, not suited to aeroacoustic investigations. Further, the assumed cylindrical deformation of the wake does not allow for capturing wake role up and wake distortion effects. Another limitation is that if the lifting line approach is used to govern the equations, the number of harmonics *m* should not exceed the number of 30 in order to avoid divergences.

Application and Validation

In the application of the Finite State Unsteady Wake model for DLR, realtime and pilot-in-the-loop aspects play a major role, since the model will be used in the ground based ACT/FHS system simulator. ONERA has put emphasis on improving the prediction capability for dynamic phenomena as *Dutch Roll* and *Ground Effect*.

Related topics to above applications, appropriate implementation aspects and model validations will be outlined subsequently.

Realtime constraints

The intended use of the Finite State Unsteady Wake model in the simulation code of the ACT/FHS system simulator makes high demands on the realtime capability of the model. In this context, the major goal is to implement the model, as far as possible, in a less time consuming way. For example, all time independent calculations are done in a pre-process. The main influence of this model, however, on time consumption comes from the number of harmonics and shapes (i.e. the number of states) taken into account for a particular simulation. This number can be freely chosen by the user depending on his particular application.

Increasing the number of model states refines the representation of the actual blade loads using the generalized forces. A more or less equally distributed pressure over the rotor disk becomes more and more a discrete pressure distribution with peaks spatially located at the rotor blades. As an example, the left pictures in **figure 1** show the difference of the resulting pressure distribution with respect to the numbers of states taken into account for EC135 helicopter in slow forward flight. In consequence of increased number of states, the resulting inflow distribution is also more expressed. As shown in the right hand side pictures of **figure 1** ,it tends from the well known trapezoidal shape (Glauert, Pitt&Peters) towards a more discrete downwash distribution with peaks at the rotor blades (or more precise, due to the unsteadiness of the model: "shortly after the blades"), and rotating with them.

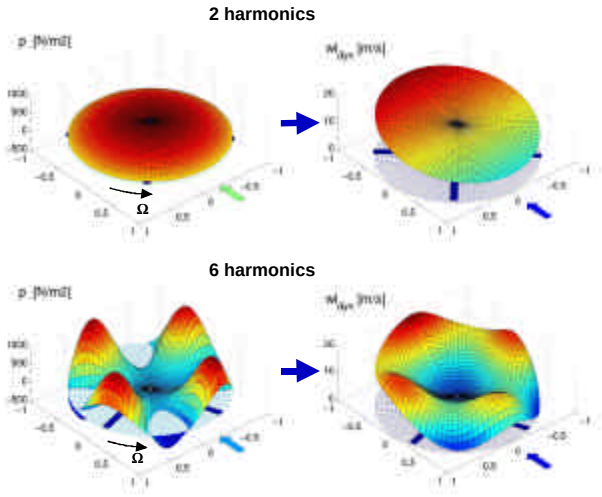

Figure 1: pressure and inflow distribution for EC135 at 10 m/s

Realtime condition is satisfied when the simulation cycle time is less than the integration step time. Simulation cycle time, i.e. the time needed to update all occurring model states for the next instance in time, depends mainly on the simulation computer CPU performance and on the complexity of the used simulation model. The integration step time is

determined for a given numerical integration method by the highest modal frequencies occurring in the model.

On increasing the number of states, the realtime condition is affected by an opposite change of the simulation cycle time and integration step size. Since for each cycle the linear equation systems of (24) and (25)have to be evaluated, simulation cycle time increases in a cubic order with the number of states. On the other hand, higher harmonic inflow state frequencies become dominant with respect to other system modes when the number of states is increased. The integration step time has to be reduced in order to avoid numerical instabilities.

Both effects are displayed in **figure 2**. The figure is based on the present status of the ACT/FHS realtime simulation configuration (w.r.t actual processor performance, model complexity, etc.). For reasons of comparison, the present integration step time is defined as 100%. For the Finite State Unsteady Wake model in Pitt&Peters configuration (i.e. 1 harmonic, 3 states) the cycle time is about 50% of the step time, thus two times realtime. On increasing the number of states to about 40, the realtime condition is no longer guaranteed. In order to stay away from the absolute bound and to have some spare for implementing other model extensions, it is suggested to use a maximum of about 25 states (i.e. about 5 harmonics). Not using inflow harmonics higher than 5 does not affect the flight dynamic simulation performance, since the frequencies incorporated with these harmonics are generally too high to play any significant role in helicopter flight dynamics.

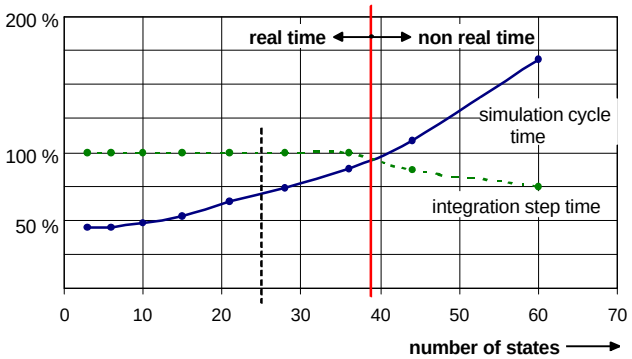

Figure 2: realtime constraints for the present ACT/FHS configuration

Effects on trim

From higher harmonic control (HHC) or individual blade control (IBC) investigations [17], it is known that a higher harmonic interfering in the aerodynamic rotor/wake equilibrium can have a remarkable influence on the helicopter trim state. Since the Finite State Unsteady Wake Model also interferes in this equilibrium, in dependence of the number of harmonics taken into account, the effect of the model complexity on the trim state is investigated. For a particular EC135 configuration trim calculations have been performed for hover, level flight at 30 m/s and at 55 m/s. For all three velocities only the number of states has been varied.

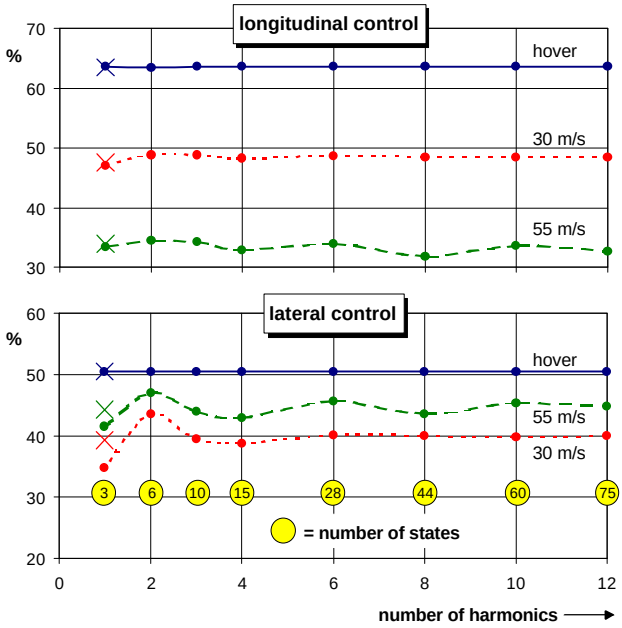

Figure 3: trim pilot controls for EC135 configuration

In **figure 3,** the results are shown for the effect on the trimmed value of longitudinal and lateral pilot control. As one can see the longitudinal control is only slightly influenced by the number of states considered in the model. The trimmed lateral control, however shows strong variations especially for forward speed and in the region with only few harmonics. The crosses in **figure 3** indicate the trim results when using the Pitt&Peters dynamic inflow model.

Due to the gyroscopical behavior of the rotor, the trim of the lateral control is mainly dependent on the longitudinal inflow distribution. Due to the wake skew the inflow is no longer symmetric in forward flight. Second and third harmonic terms seem to interfere with the rotor/wake equilibrium in different ways.

In the Pitt&Peters model, a correction is performed to take into account the influence of higher order shape functions in only 3 states. The Finite State Unsteady Wake model does not have this correction when only using 3 states. However, considering more than about 3 harmonics (i.e. 10 states) this correction is automatically included. As can be seen from **figure 3,**

lateral control trim values for this case correspond with Pitt&Peters values.

The trim value of the collective control is directly linked to the mean momentum inflow. Because of the orthogonality of inflow states, the higher harmonic terms have no contribution to the mean inflow, and thus do not affect the trim value of the collective control. Also, pedal control trim used mainly to compensate for rotor torque shows no variation with the number of states considered.

Summarizing the results, it seems reasonable for flight dynamic applications to use the model with a minimum of 15 states (i.e. 4 harmonics). The number of states then no longer has influence on the helicopter trim attitude.

Definition of reference frame

The basic Finite State Unsteady Wake model has been formulated to describe the inflow distribution of a lifting rotor in hover, axial or forward flight. The equation system is evaluated in a reference frame which is aligned with the inflow direction (i.e. the wind axes system), as shown in **figure 4**. The description does not basically count for any hub motion other than translational motion in wind axis direction. In practical helicopter flight dynamic simulation, the hub motion, however, in arbitrary translational as well as rotational sense can not be neglected. For example, the effects of distorting the wake due to pitch and roll motion of the rotor (i.e. rotating the reference system about the x and y axes) play an important role on the prediction of helicopter cross-coupling behavior. The "parametric wake distortion" formulation (see next paragraph) is used to extend the inflow model to account for these phenomena.

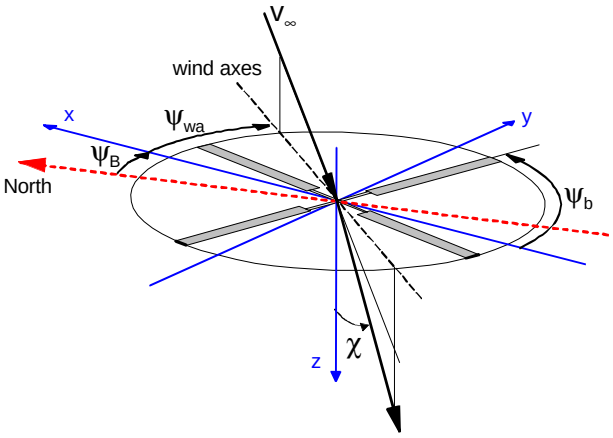

Figure 4: reference frame and angle definition

The influence of sideward hub motion or a yaw motion of the reference system (i.e. rotation about the z-axis), however, is still not considered. To overcome both problems, a reference system other than the wind axes frame has to be used. In [18] for the Pitt&Peters inflow model, a formulation is derived which uses the rotor frame as reference system. Going one step further, here it is proposed to use the geodetic (earth fixed) inertial system as reference. The advantage of this formulation is that the integration of the inflow state derivatives is performed in a fixed and non rotating system. No effects due to integrating in a moving reference system occur. It has to be mentioned that this holds true only when helicopter roll and pitch attitudes do not become too large.

As shown in **figure 4,** the geodetic *North* axis is taken as reference. The system described in equations (24) and (25) is still evaluated in the wind axes frame. The integration of derivatives, however, is performed with respect to the North axis. In practice, this means that the inflow states after integration have to transformed into the wind axes system using a rotation matrix *T*:

$$\begin{pmatrix} \alpha_n^m \\ \beta_n^m \end{pmatrix}_{wa} = \begin{pmatrix} \cos m\psi_{abs} & -\sin m\psi_{abs} \\ \sin m\psi_{abs} & \cos m\psi_{abs} \end{pmatrix} \cdot \begin{pmatrix} \alpha_n^m \\ \beta_n^m \end{pmatrix} = T \cdot \begin{pmatrix} \alpha_n^m \\ \beta_n^m \end{pmatrix} \quad (32)$$

where $\psi_{abs} = \psi_B + \psi_{wa}$ the angle between reference axis and wind axis. The index *wa* marks the inflow states in wind axes frame. The resulting derivatives then have to be transformed back in a similar way by using:

$$\begin{pmatrix} \dot{\alpha}_n^m \\ \dot{\beta}_n^m \end{pmatrix} = T^{-1} \cdot \begin{pmatrix} \dot{\alpha}_n^m \\ \dot{\beta}_n^m \end{pmatrix}_{wa} + \dot{T}^{-1} \cdot \begin{pmatrix} \alpha_n^m \\ \beta_n^m \end{pmatrix}_{wa} \quad (33)$$

To calculate the generalized forces in equations (30) and (31) the angle $\psi_{rel} = \psi_b + \psi_{wa}$ has to used instead of ψ_b. Finally, to obtain the present inflow at the blade element location, equation (10) has to be evaluated using the wind axes inflow states from (32) and the angle ψ_{rel} as reference angle.

Wake distortion

As mentioned before, a rotation of the helicopter about the roll or pitch axis results in a bending of the induced wake. The induced flow field now at the rotor disk is distorted in such a way that it can be interpreted as if an additional trapezoidal inflow gradient is superposed on the induced flow. Due to the gyroscopical behavior of the rotor disk, the helicopter dynamic response to such an inflow gradient occurs mainly in the off-axis. The

wake distortion effect, thus, has an important influence on helicopter cross-coupling prediction.

For practical use, in flight dynamic simulation parametric models are derived to take into account the wake distortion effects. In a first approach here, a similar extension as proposed for the Pitt&Peters model is implemented. Tip path plane motion dependent linear perturbation terms are included in equations (24) and (25):

$$\left(\bar{\bar{L}}^{r\,m\,c}_{j\,n}\right)\cdot\overset{*}{\bar{\alpha}}^{r}_{j} = -V^{m}_{n}\cdot\left(\bar{\alpha}^{r}_{j}-\bar{\alpha}^{r}_{j,\,wd}\right)+\left(\bar{\bar{L}}^{r\,m\,c}_{j\,n}\right)\cdot\bar{\tau}^{m\,c}_{n} \qquad (34)$$

$$\left(\bar{\bar{L}}^{r\,m\,s}_{j\,n}\right)\cdot\overset{*}{\bar{\beta}}^{r}_{j} = -V^{m}_{n}\cdot\left(\bar{\beta}^{r}_{j}-\bar{\beta}^{r}_{j,wd}\right)+\left(\bar{\bar{L}}^{r\,m\,s}_{j\,n}\right)\cdot\bar{\tau}^{m\,s}_{n} \qquad (35)$$

where $\bar{\alpha}^{r}_{j,\,wd}$ and $\beta^{r}_{j,\,wd}$ count for the additional inflow gradient. Since in this simplified approach only the first harmonic distortion components are considered, the distortion states are only non-zero when $r=1$ and $j=2$:

$$\bar{\alpha}^{1}_{2,\,wd} = \frac{K_q\cdot q_{TPP}}{\Omega\cdot\left.\dfrac{\bar{P}^{1}_{2}(\nu)}{\nu}\right|_{\nu=0}} \quad , \quad \bar{\beta}^{1}_{2,\,wd} = \frac{K_p\cdot p_{TPP}}{\Omega\cdot\left.\dfrac{\bar{P}^{1}_{2}(\nu)}{\nu}\right|_{\nu=0}} \qquad (36)$$

The values of the gain factors K_p and K_q in above equations have been subject to extensive theoretical investigations (e.g. [2], [19]). Also, parametric optimization methods can be applied to estimate the gain factors [20]. In general, it is agreed on $K_p = K_q = 1.5$ for the hover case. In forward flight both, factors decrease but in different measures depending on the theory or method used to determine them.

Validation and results

At DLR an extensive flight test data base for the BO105 helicopter exists. The data are used for identification, model validation and handling qualities research purposes. Since, for the moment, only limited flight test data for the EC135 are available, the validation of the realtime code for the ACT/FHS system simulator is mainly performed in BO105 configuration using the existing BO105 data base.

The helicopter model used for the validation runs incorporates a 6 DOF rigid body formulation, main rotor rigid blade flapping and lagging, local blade element aerodynamic, wake interference on fuselage tail components and a dynamic engine representation. For the induced velocity, the 3-state Pitt&Peters and the Finite State Unsteady Wake model are available, both with geodetic reference axis and parametric wake distortion extension.

In **figure 5,** a lateral 3211 cyclic control was applied to a BO105 helicopter in hover. The thick solid line represents the flight measured data. The dashed line represents the simulation results using the Pitt&Peters formulation, whereas the thin solid line shows the results for the Finite State Unsteady Wake approach with 4 harmonics (i.e. 15 states). For both models, the wake distortion factors are set to $K_p = K_q = 1.5$.

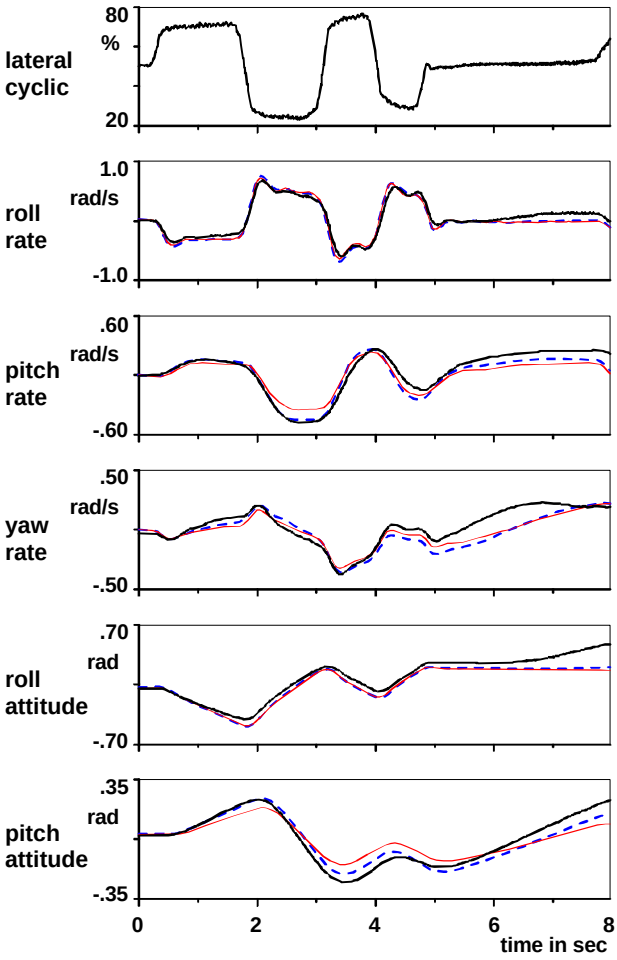

Figure 5: lateral 3-2-1-1 for BO105 in hover

In the on-axis roll response prediction, both model formulations perform very well. In the off-axis pitch response, the damping of the Finite State Unsteady Wake model seems to be higher than the one in the Pitt&Peters formulation. The latter, therefore, gives a better prediction of the cross-coupling response. A possible cause might be that the relatively simple parametric wake distortion extension of (34) to (36) is not appropriate for such a complex formulation as the Finite State Unsteady Wake model. This may indicate that in combination with this model more sophisticated wake distortion formulations, as presented in [9], have to be used.

In the yaw axis, however, the damping in the Pitt&Peters model is too low and the Finite State model performs better. This is probably due to the more correct unsteady inflow representation in rotational sense which provides a better interaction between the "rotating" dynamic higher harmonic states in combination with the dynamic engine model.

Figure 6 compares the flight test data (thick solid line) to the simulation results for a longitudinal 3211 cyclic control input at 100 kts forward. The wake distortion parameters are set to $K_p = K_q = 0.5$. Again, the comparison between the Pitt&Peters formulation (dashed line) and the Finite State Unsteady Wake model with 15 states (thin solid line) is performed.

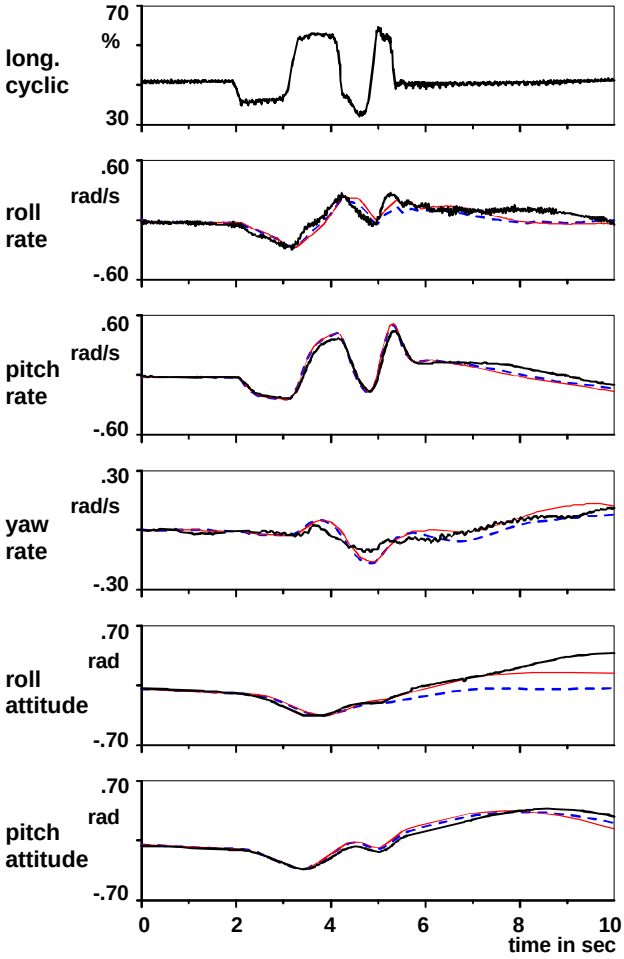

Figure 6: longitudinal 3-2-1-1 for BO105 at 100 kts

Both dynamic inflow representations show a similar result for the on-axis pitch response which is slightly overpredicted. In the off-axis roll response, the Finite State Unsteady Wake model is able to match flight test data slightly better. This results in less drift in the roll attitude, occurring after about 5 sec. It has to be mentioned that the values for the wake distortion parameters used in this simulation are higher than the theoretical values derived for forward flight (≈ 0). The considered values, however, allow for a better cross-coupling prediction. The yaw axis response is overpredicted by both formulations which might be due to the not well predicted higher order dynamics in the engine model for high forward speeds.

In general, both dynamic inflow formulations applied in helicopter flight dynamic simulation are able to correctly predict the on-axis response to pilot control inputs for hover as well as forward flight. Taking into account the parametric wake distortion extension, the correct tendencies in the off-axis cross-coupling behavior could also be predicted, although considering a more sophisticated wake distortion approach for the Finite State Unsteady Wake model could even improve the results.

Rotor wake interferences

The extension of the Finite State Unsteady Wake model to compute of the induced velocities outside of the rotor has been studied at ONERA this year. The purpose is to apply it to calculate the rotor wake interferences on the rear components (horizontal and vertical tails, tail rotor) and to use it for time simulations. More precisely, the basic helicopter model overestimates the damping of the “Dutch-roll mode”. By modeling the aerodynamic perturbations of the main rotor wake on the tail components, the oscillations on the 3 axes (yaw-roll-pitch) could be better predicted.

Model extension

For the computation of the induced velocities outside the rotor, it is assumed that they are mainly due to the convection phenomenon. The unsteady part of the momentum equation is neglected. For our application, this seems to be a reasonable assumption, since the tail components are rather close to the rotor and the convection time from the rotor down to these elements may be negligible. For calculating the induced velocities outside the rotor disk equation (15) is used for all coordinate directions:

$$v_i = -\frac{1}{V_\infty}\int_0^\infty \frac{\partial \Phi^V}{\partial e_i} d\xi \qquad (37)$$

The induced velocity at any point in space is calculated by integrating the spatial derivatives of the pressure function along a streamline parallel to the mean wake line. This integration is performed from the considered

point to the infinite upstream (in practice up to a distance equal to 15 rotor radius).

Figure 13 shows the ellipsoidal coordinates associated with the rotor-wind frame (the z-axis is along the rotor shaft and the x-axis is in the wind horizontal direction, the deviation from the x-rotor-axis is given by the sideslip angle). The induced velocity components are first calculated in the relative-wind frame (x_ξ, y_ξ, z_ξ) in which the x-axis is in the direction of the relative wind. Compared to the previous rotor-wind frame (**figure 13**), a rotation is applied around the common y-axis with the rotor angle of attack $\alpha = \pi/2 - \chi$.

Induced velocity components

The formulation of the induced velocity component in the streamline direction x_ξ in the relative-wind-frame does not require any integration of (37). The acceleration potential tends to zero at the upstream infinite and is discontinuous across the rotor. That is why two kinds of calculations are performed if the considered point is outside or inside the wake. Outside the wake :

$$u_\xi = -\frac{1}{V_\infty}\Phi^V_\xi \qquad (38)$$

Inside the wake, the pressure discontinuity through the rotor disc must be taken into account :

$$u_\xi = \frac{1}{V_\infty}\left[\Phi^V_{\xi=0^-} - \Phi^V_{\xi=0^+} - \Phi^V_\xi\right] \qquad (39)$$

The induced velocity in y_ξ direction is obtained by integrating the lateral component of equation (37):

$$v_\xi = \frac{1}{2V_\infty}\sum_{m=0}^{\infty}\sum_{\substack{n=m+1,\\ m+3,..}}^{\infty}\left(v^{mc}_{n\ y}\cdot\tau^{mcV}_n + v^{ms}_{n\ y}\cdot\tau^{msV}_n\right) \qquad (40)$$

where $\tau^{mc\,V}_n$ and $\tau^{ms\,V}_n$ are the convection parts of the generalized forces. The coefficients $v^{mc}_{n\ y}$ and $v^{ms}_{n\ y}$ depend on the geometry of the problem:

$$v^{mc}_{n\ y} = \int_\xi^\infty \frac{\partial}{\partial y_\xi}\left(\bar{P}^m_n(\nu)\bar{Q}^m_n(i\eta)\cos m\psi\right)d\xi \qquad (41)$$

$$v^{ms}_{n\ y} = \int_\xi^\infty \frac{\partial}{\partial y_\xi}\left(\bar{P}^m_n(\nu)\bar{Q}^m_n(i\eta)\sin m\psi\right)d\xi \qquad (42)$$

The expression for the cartesian derivative $\partial/\partial y_\xi$ in the rotor ellipsoidal coordinate system is explained in the appendix.

The same kind of formulation as in (40) is applied for the velocity component in z_ξ direction:

$$w_\xi = \frac{1}{2V_\infty}\sum_{m=0}^{\infty}\sum_{\substack{n=m+1,\\ m+3,..}}^{\infty}\left(v^{mc}_{n\ z}\cdot\tau^{mcV}_n + v^{ms}_{n\ z}\cdot\tau^{msV}_n\right) \qquad (43)$$

with a similar approach for $v^{mc}_{n\ z}$ and $v^{ms}_{n\ z}$ as displayed in (41) and (42). Compared to the v_ξ-component, here one more rotation (i.e. about the rotor angle of attack) has to be performed to obtain $\partial/\partial z_\xi$ (see appendix).

Now the 3-components of the induced velocity by the main rotor can be calculated at the center of each tail elements (horizontal stabilizer, fin, tail rotor). They are finally transferred in the appropriate frame.

Steady induced velocity fields

For the isolated main rotor of the Dauphin helicopter, the induced velocity fields have been computed with the extended Finite State Unsteady Wake model in hover and forward flight. In hover, as can be seen on **figure 7**, the main patterns of the rotor induced velocity field are caught with only one inflow state α^0_1. The axissymmetrical flow is accelerated downward through the rotor leading to the well-known radial contraction.

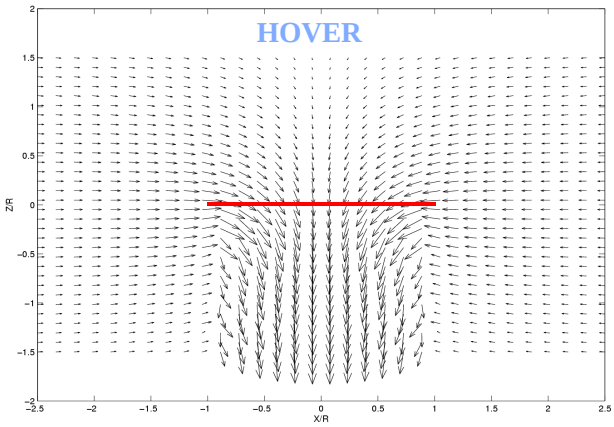

Figure 7: induced velocity field of a hovering rotor

In forward flight, more inflow states must be used in order to represent the changes in the induced flow due to the fact that the wake is skewed backward. With the following 6 inflow states $\alpha^0_1, \alpha^0_3, \alpha^1_2, \alpha^1_4, \beta^1_2, \beta^1_4$, the expected induced flow in forward flight is obtained as shown in the following **figure 8**.

The downwash predominance inside the wake, makes appear the skewed wake. The strongest downwash is under the back part of the rotor, whereas a recirculation under the front part leads to a small upwash tendency. These characteristics are quite correlated with those

observed in experimental studies, as well as with other numerical approaches like the vortex methods [12].

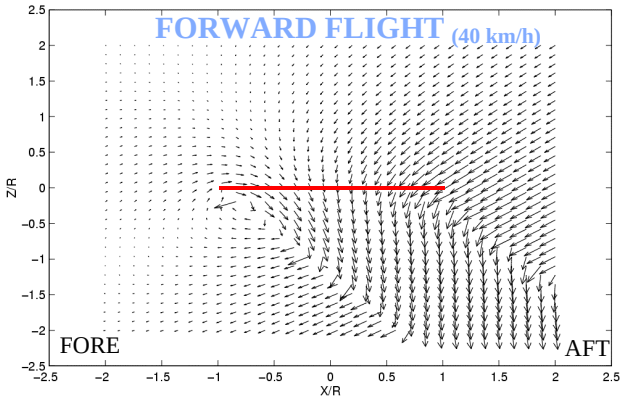

Figure 8: induced velocity field in forward flight

Dynamic simulation results

Most of the helicopter simulation codes underestimate the oscillations around the 3-axes (yaw-roll-pitch) associated with the "Dutch-roll" behavior [21]. A flight test campaign dedicated to this problem was lead on a Dauphin helicopter by the French Flight Test Center (CEV) based in Istres. Here, only one example illustrating the extensive comparisons performed between the HOST code simulations and this flight data base is shown.

The overestimation of the damping of the "Dutch-roll" motions (following the doublet input on the pedals) can be seen in **figure 9** when considering the simulation results (in red) obtained with the basic Finite State Unsteady Wake model, for which as previously the 6 inflow states: $\alpha_1^0, \alpha_3^0, \alpha_2^1, \alpha_4^1, \beta_2^1, \beta_4^1$ are used.

By adding the interference phenomena induced by the main rotor wake on the tail rotor and the fin, the oscillations on the yaw and the roll axes are better simulated (curves in green on **figure 9**). However, they are overestimated in magnitude and are in advance compared to the test data. But this is mainly due to the fenestron model. Its too high sensitivity to pedal inputs appears clearly during the doublet excitation (see the yaw rate RHEL).

On the pitch motion the oscillations are still underestimated (see QHEL). When the induced velocities by the main rotor wake on the horizontal stabilizer are taken into account with the extended Finite State Unsteady Wake model or the vortex rings model [22], the pitch oscillations are not generally better simulated. The predicted downwash produces sometimes a pitch-up motion which makes the simulation diverge after 15 sec.

Indeed the pitch oscillations are clearly correlated with the roll motion and it appears that the pitch oscillations

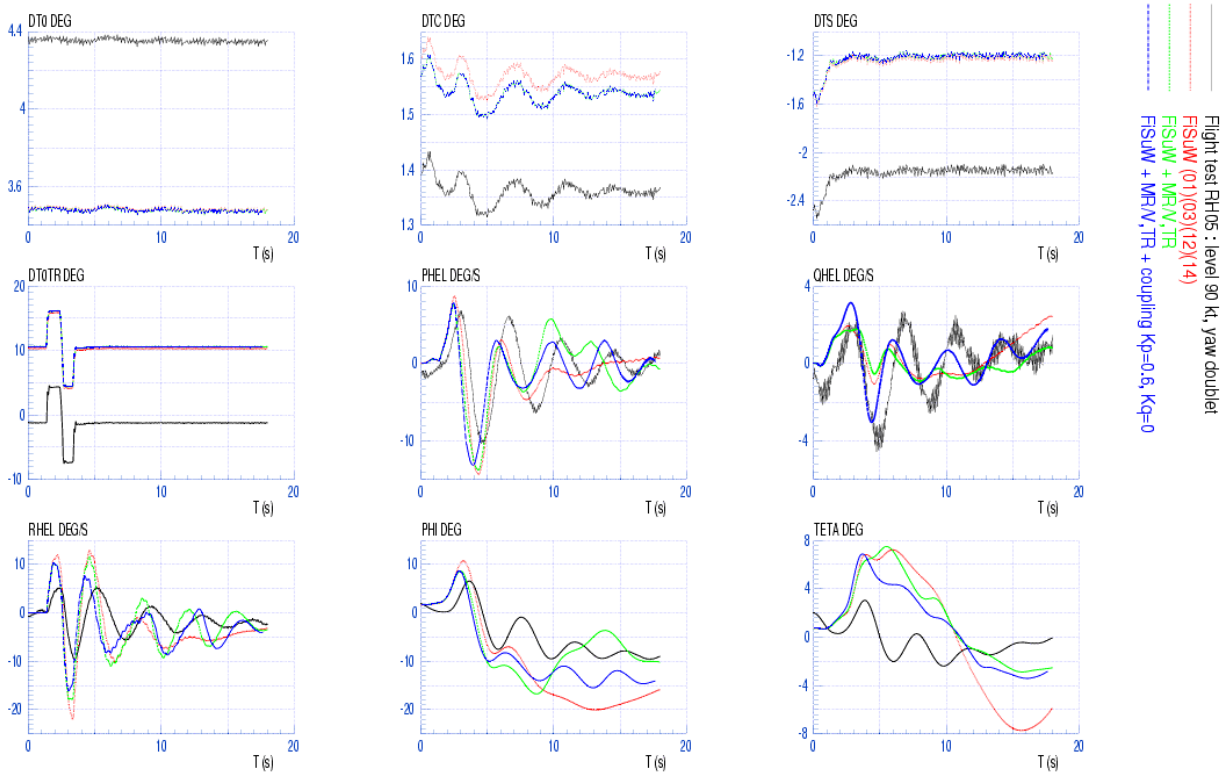

Figure 9: Dutch-roll motions after a doublet pedal input for the Dauphin in level flight at 90 kts

in the Dutch-roll are probably rather due to the roll-pitch cross-coupling than to rotor wake interference on the horizontal tail.

To take into account the linear longitudinal and lateral inflow gradients due to tip path plane motion ONERA uses a similar wake distortion approach as derived in (34) to (36). In hover, the value of the coefficients K_p and K_q can be taken around 1.5 . But in forward flight, they decrease due to the fact that the rotor wake is swept backwards. If these new terms are interpreted as representing the rotor wake distortion effects, they should be neglected above $m = 0.15$ according to the study reported in [19]. Nevertheless, they provide an efficient way to better simulate the pitch-roll coupling, (even if their physical interpretation can not be reduced to the wake distortion in forward flight).

A parametric study on the Dutch-roll database shows that with $K_p \approx 0.5$, $K_q = 0$, the coupling from the roll to the pitch is generally better simulated. On **figure 9**, the results (in blue) obtained with both: the interferences on the fin and the tail rotor, and the inflow coupling terms with $K_p \approx 0.6$ and $K_q = 0$ illustrate the improvements especially on the pitch oscillations. They are due to the change in the lateral inflow gradient b_2^1 produced by the roll motion.

As a by product of the improvement in the pitch axis, the oscillations are also better calculated in magnitude and phase in the yaw and roll axes. This interesting corollary may be due to the change in the interferences, since the pitch attitude and wake skew angle are modified, as seen from **figure 10**.

Conclusion about the Dutch-Roll simulation

The Finite State Unsteady Wake model has been extended to compute the induced velocities by the main rotor wake anywhere in theory and in practice on the tail components. New terms have also been introduced in the main rotor dynamic inflow equations to account for the effect of the pitch and roll motions on the longitudinal and lateral inflow gradients.

A better prediction of the Dutch-roll oscillations can be achieved by calculating the interferences on the fin and on tail rotor with Finite State Unsteady Wake model, and by representing the roll to pitch coupling with $K_p \approx 0.5$, $K_q = 0$.

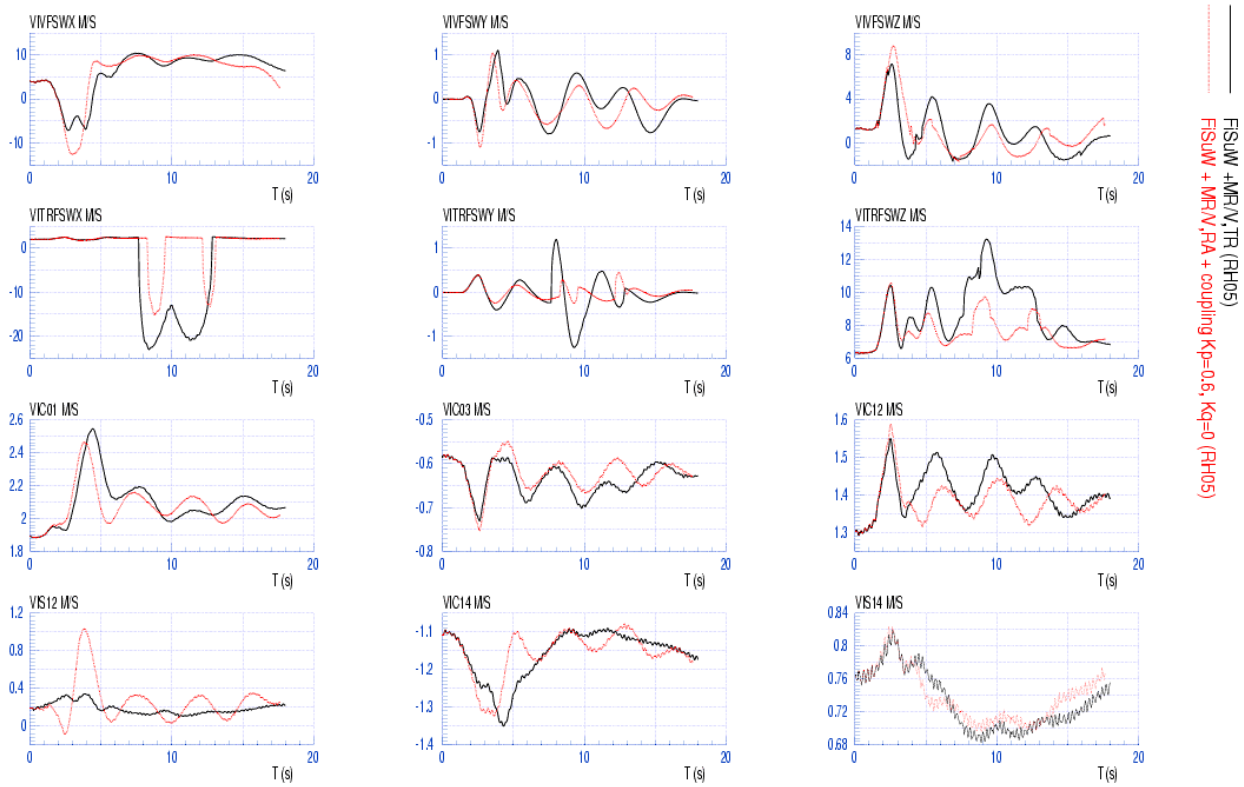

Figure 10: induced velocities on fin (ViV_FSW), tail rotor (ViTR_FSW) and main rotor, Dauphin at 90 kts

Further improvements could be achieved by upgrading the fenestron model and by using a parametric optimization tool to determine the best couple of K_p and K_q, on the Dutch-roll database.

Ground effect

The interference of the rotor flow with the ground changes the velocity and pressure distributions around the blades, and thus the airloads. Typically, for a rotor hovering near the ground $(H_{alt} < R)$, the mean down wash is reduced due to the increase of the pressure between the rotor and the ground. Therefore, the induced power decreases and the required power is lower compared to the case where the rotor is out of ground effect.

In [10], [11], [23] an extension to the Finite State Unsteady Wake model is proposed which allows to take into account the ground effect not only on the mean down wash, but also on the other inflow states. Indeed, as soon as the rotor wake is not normal both to the rotor and the ground, (e.g. in forward flight or when the rotor and the ground are not parallel), the effects on the rotor inflow distribution will not be uniform. This year ONERA has implemented these extensions in HOST.

Model extension

The ground effect is represented as a second source of perturbation of the pressure field, depending on the first one coming from the rotor. In analogy to (6), the additional pressure function can be written as:

$$\Phi_G = -\frac{1}{2}\sum_{l=0}^{\infty}\sum_{\substack{k=l \\ l+2,..}}^{\infty} \bar{P}_k^l(\hat{\nu})\cdot\bar{Q}_k^l(i\hat{\eta})\cdot \cdot\left(\sigma_k^{lc}(\bar{t})\cos l\psi + \sigma_k^{ls}(\bar{t})\sin l\psi\right) \tag{44}$$

where the hats indicate the states with respect to the inclined ground frame, as shown in **figure 11**. The σ_k^{lc} and σ_k^{ls} denote the generalized forces due to the ground. Further, it should be mentioned that in contrast to (6) $k+l = even$, thus $k = l,\quad k = l+2,\cdots$. The total pressure perturbation, which determines the rotor inflow distribution, is viewed as the superposition of both the rotor and ground contributions: $\Phi = \Phi_R + \Phi_G$. Here again it is assumed that only the convection part of the pressure function plays a significant role, thus neglecting the unsteady part. The pressure potential must lead at the ground level to an airflow with a null component normal to the ground surface.

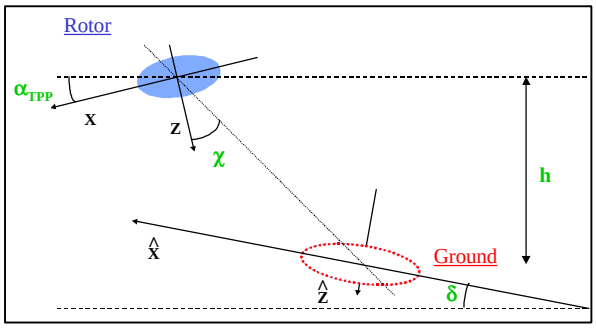

Figure 11: helicopter-, wake- and inclined ground frame

A matrix C joins up the ground pressure coefficients with those of the rotor. This matrix is calculated through a double integration, and using the transformations between the ellipsoidal coordinates in the ground frame $(\hat{\nu},\hat{\eta},\hat{\psi})$ and in the rotor frame:

$$\sigma_k^{lc} = C_{kn}^{lmc}\cdot\tau_n^{mc} \tag{45}$$

$$\sigma_k^{ls} = C_{kn}^{lms}\cdot\tau_n^{ms} \tag{46}$$

with:

$$C_{kn}^{lmc} = -\frac{1}{\delta\pi}\int_0^{2\pi}\int_0^1 \bar{P}_k^l(\hat{\nu})\cos l\hat{\psi}\cdot\left(\bar{P}_n^m(\nu)\bar{Q}_n^m(i\eta)\right) \cdot\cos m\psi\, d\hat{\nu}d\hat{\psi} \tag{47}$$

$$C_{kn}^{lms} = -\frac{1}{\pi}\int_0^{2\pi}\int_0^1 \bar{P}_k^l(\hat{\nu})\sin l\hat{\psi}\cdot\left(\bar{P}_n^m(\nu)\bar{Q}_n^m(i\eta)\right) \cdot\sin m\psi\, d\hat{\nu}d\hat{\psi} \tag{48}$$

The induced velocities due to the ground potential (44) can then be expressed as:

$$\hat{\alpha}_{jG}^r = V^{-1}\cdot\hat{D}_{jk}^{rlc}\cdot\frac{1}{2}\sigma_k^{lc} \tag{49}$$

$$\hat{\beta}_{jG}^r = V^{-1}\cdot\hat{D}_{jk}^{rls}\cdot\frac{1}{2}\sigma_k^{ls} \tag{50}$$

The expansion of the matrix D elements is very similar to the one given in (19) and (20).

Evaluation of equations (45) to (50) shows that matrices C and D can be combined to a matrix G. The ground effect extension can now be introduced in the overall inflow formulation from (21) and (22):

$$M\cdot\overset{*}{\alpha}_j^r + \left(\hat{L}_{jn}^{rmc} - G^c\right)^{-1}\cdot V\cdot\hat{\alpha}_j^r = \frac{1}{2}\tau_n^{mc} \tag{51}$$

$$M\cdot\overset{*}{\beta}_j^r + \left(\hat{L}_{jn}^{rms} - G^s\right)^{-1}\cdot V\cdot\hat{\beta}_j^r = \frac{1}{2}\tau_n^{ms} \tag{52}$$

Results for ground effect in hover

For the case of hover above an inclined ground, the model extensions have been compared with the results

presented in [11]. Since a good match with these results could be achieved, the validation seems to be fulfilled.

Results for ground effect in forward flight

In order to reduce the computational time during the trim process of the whole helicopter for a sweep on the forward speed, the number of combinations describing the airloads and induced velocity distributions on the rotor and the ground is diminished, i.e. rotor states: $\tau_1^{0c}, \tau_2^{1c}, \tau_2^{1s}, \alpha_1^0, \alpha_2^1, \beta_2^1$. ground states: $\sigma_0^{0c}, \alpha_{0G}^0$

In forward flight, as proposed in [11], an effective wake skew angle χ_e is used to compute the *G* matrix in order to account for the roll-up of the wake:

$$\tan\chi_e = \frac{\pi^2}{4}\tan\chi \qquad (53)$$

Figure 12 shows the evolution with the forward speed of the induced power IGE (*h*=0.71). The induced power is made non-dimensional by dividing its values by the hover induced power IGE. The advance ratio is normalized with the non-dimensional mean inflow in hover according to the momentum theory:

$$\mu^* = \mu \cdot \sqrt{2/c_t} \qquad (54)$$

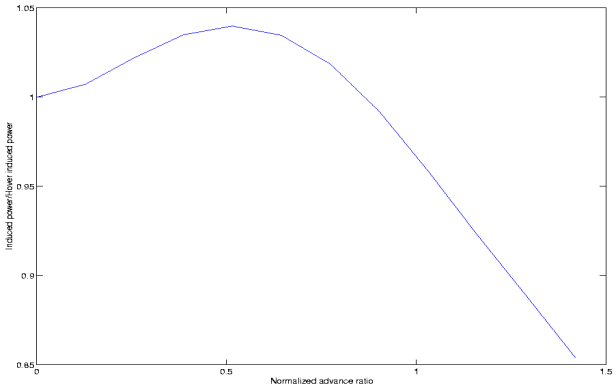

Figure 12: induced power IGE (*h*=0.71)

As can be seen on **figure 12**, the reduction of rotor inflow due to the ground effect is stronger in hover than in forward flight. That is why the induced power IGE increases at low forward speeds compared to the value in hover. The drop down corresponding to the decrease of the mean down wash with the forward speed becomes more important, and thus the induced power falls down as in the well-known OGE case. This non-linear behavior is well correlated with the experimental data from [24] and with the numerical results of [11].

Conclusion about the ground effect modeling

In hover above a flat or inclined ground, the validation of the model seems to be fulfilled. In forward flight, when using more refined combinations to the describe the rotor and ground distributions, the model may appear time consuming and some problems of convergence may occur during the equilibrium process. Nevertheless, the most important effects are caught by the model when using the first states (mean terms and first harmonic gradients), corresponding to the combinations applied here.

General conclusions

The Finite State Unsteady Wake model has been implemented in the helicopter flight dynamic simulation codes at ONERA and DLR. The implementation was verified using generic data provided by NLR generated with the FlightLab simulation tool.

ONERA concentrated on improving the prediction capability for dynamic phenomena as *Dutch Roll* and *Ground Effect*. For this, additional model extension to account for the wake distortion effect and to calculate the induced flow at an arbitrary point outside the rotor disk were implemented. Validation with Dauphin helicopter flight test data showed that improvement in the Dutch roll oscillation prediction could be achieved.

DLR investigated aspects related to the application of the model in the ACT/HS realtime, pilot-in-the-loop simulation environment. An optimum number of harmonics and states was derived which allowed for an accurate inflow distribution calculation, but still satisfied realtime constraints. Additional extensions for parametric wake distortion and reference axis transformation were implemented. Comparison of simulation results with BO105 flight test data shows that the Finite State Unsteady Wake model performs well in hover as well as forward flight.

Although the model considers more dynamic inflow states the performance, was not remarkably better than the 3-state Pitt&Peters formulation. It seems that in order to be fully effective, the sophisticated complex model formulation demands to be equaled by equivalent complex formulations for dynamic components as the rotor system (e.g. elastic blade deformation), the fenestron or wake distortion.

Acknowledgement

In order to validate the implementation of the Finite State Unsteady Wake model, NLR made available simulation data generated with FlightLab for ONERA and DLR. We wish to thank NLR for this contribution.

The ONERA's part of the work has been supported by the French Ministery of Defense (SPAe).

References

[1] Pitt, D.M. and Peters, D.A., *"Rotor Dynamic Inflow Derivatives and Time Constants From Various Inflow Models"*, 9th European Rotorcraft Forum, Stresa, Italy, 1983.

[2] Kothmann, B.D., Keller, J.D. and Curtiss, H.C., *"On Aerodynamic modelling for rotorcraft Flight Dynamics"*, 22nd European Rotorcraft Forum, Brighton, UK, September 17-19, 1996.

[3] Basset, P.-M., *"Contributions to the Improvement of a Simulation Model of Helicopter Flight Mechanics"*, Doctoral Thesis of the Mediterranean University, Aix-Marseille II, 29 September, 1995.

[4] Hamers, M. and Grünhagen, W. von, *"Nonlinear Helicopter Model Validation Applied to Realtime Simulations"*, American Helicopter Society 53rd Annual Forum, Virginia Beach, Virginia, April 29 - May 1, 1997.

[5] Peters, D.A. and He, C.J., *"A Closed-Form Aerodynamic Theory for Lifting Rotors in Hover and Forward Flight"*, American Helicopter Society 43rd Annual Forum, Saint Louis, Missouri, May 18 - 20, 1987.

[6] He, C.J., *"Development and Application of a Generalized Dynamic Wake Theory for Lifting Rotors"*, Ph.D. Dissertation, Georgia Institute of Technology, August, 1989.

[7] Du Val, R. and He. C.J., *"Integration of Simulation Validation Tools with a Comprehensive Rotorcraft Analysis for Physically-Based Validation with a Comprehensive Rotorcraft Analysis"*, AHS Vertical Lift and Design Conference, San Francisco, California, January 19 – 21, 2000.

[8] He, C.J., *"Finite State Dynamic Wake Interference Modeling for Rotorcraft Simulation"*, American Helicopter Society 53rd Annual Forum, Virginia Beach, Virginia, April 29 - May 1, 1997.

[9] Krothapalli, K.R., Prasad, J.V.R. and Peters, D.A., *"A Generalized dynamic Wake Model with Wake Distortion Effects"*, American Helicopter Society 54rd Annual Forum, Washington, D.C., May 20 - 22, 1998.

[10] Xin, H., Prasad, J. V. R. and Peters, D. A., *"Ground Effect Aerodynamics of Lifting Rotors Hovering Above Inclined Ground Plane"*, presented at the AIAA 17th Applied Aerodynamics Conference, Norfolk, Virginia, June 1999.

[11] Xin, H., Prasad, J. V. R. and Peters, D. A., *"Dynamic Inflow Modeling for Simulation of a Helicopter operating in Ground Effect"*, presented at the AIAA Modeling and Simulation Technology Conference, Portland, Oregon, August, 1999.

[12] Benoit, B., Dequin, A.-M., Basset, P.-M., Gimonet, B., Grünhagen, W. von, Kampa, K., *"HOST, a General Helicopter Simulation Tool for Germany and France"*, American Helicopter Society 56th Annual Forum, Virginia Beach, Virginia, May 2 – 4, 2000.

[13] Hamers, M., Bouwer, G. and Grünhagen, W. von, *"System Simulator for the DLR's Inflight Simulator ACT/FHS –Software and Hardware Realisations-"*, AHS Vertical Lift and Design Conference, San Francisco, California, January 19 – 21, 2000.

[14] Peters, D.A. and He, C.J., *"Correlation of Measured Induced Velocities with a Finite State Wake Model"*, Journal of the American Helicopter Society, Vol. 36, 1991.

[15] Peters, D.A. and He, C.J., *"Finite State Induced Flow Models – Part II: Three-Dimensional Rotor Disk"*, Journal of Aircraft, Vol. 32, No. 2, March-April, 1995.

[16] Kinner, W., *"Die Kreisförmige Tragflache auf Potentialtheoretischer Grundlage"*, Ingenieur Archiv, Vol 7, 1937.

[17] Höffinger, M.T., *"Beeinflussung der Hub-schrauber- Flugeigenschaften durch Aktive Rotorsteuerung"*, Diplom Thesis at DLR Braunschweig, Juli, 2000.

[18] Peters, D.A. and HaQuang, N., *"Dynamic Inflow for Practical Application"*, Journal of the American Helicopter Society, Vol. 33, No. 4, October, 1988.

[19] Basset, P.-M., Tchen-Fo, F., *"Study of the Rotor Wake Distortion Effects on the Helicopter Pitch-Roll Cross-Coupling"*, 24th European Rotorcraft Forum, Marseilles, France, September 15-17, 1998.

[20] Krämer, Ph. and Gimonet, B., *"Improvement of Nonlinear Simulation Using Parameter Estimation Techniques"*, 26th European Rotorcraft Forum, The Hague, The Netherlands, September 26-29, 2000.

[21] Prouty, R.W., *"The Peculiarities of the Dutch-Roll"*, Rotor and Wings International, June, 1992.

[22] Basset, P.-M., El Omari, A., *"A Rotor Vortex Wake Model for Helicopter Flight Mechanics and its Application to the Prediction of the Pitch-Up Phenomenon"*, 25th European Rotorcraft Forum, Rome, Italy, September 14-16, 1999.

[23] Prasad, J.V.R., Zhang, H. and Peters, D.A., *"Finite State In-Ground Effect Inflow Models for Lifting Rotors"*, American Helicopter Society 53rd Annual Forum, Virginia Beach, April 29 - May 1, 1997.

[24] Huston, R.J. and Morris, C.E., *"A Wind-Tunnel Investigation of Helicopter Directional Control in Rearward Flight in Ground Effect"*, NASA TN D-6118, 1971.

Appendix

The appendix describes briefly the ellipsoidal coordinate frame and several formulations which are used in the paper.

Ellipsoidal coordinates

The ellipsoidal coordinate system as shown in **figure 13** can be described by:

$$x = -\sqrt{1-\nu^2}\cdot\sqrt{1+\eta^2}\cdot\cos\psi \tag{55}$$

$$y = -\sqrt{1-\nu^2}\cdot\sqrt{1+\eta^2}\cdot\sin\psi \tag{56}$$

$$z = -\nu\cdot\eta \tag{57}$$

with: $-1\le\nu\le1,\ 0\le\eta\le\infty$ and $0\le\psi\le2\pi$.

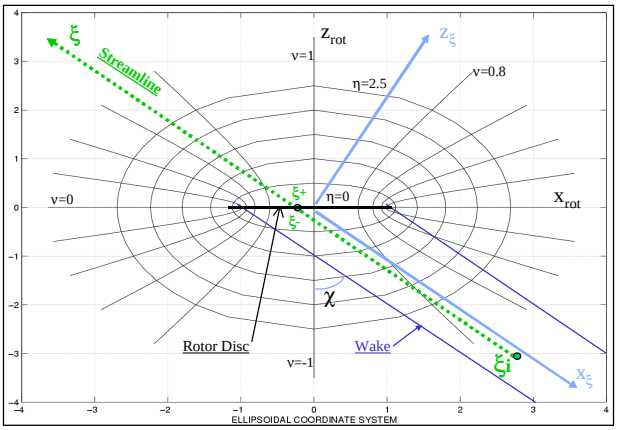

Figure 13: ellipsoidal frame and relative wind frame

The non dimensional rotor radius at disk level $(\eta=0)$ then is:

$$r = \sqrt{x^2+y^2} = \sqrt{1-\nu^2} \tag{58}$$

Further the expression of the cartesian derivative $\partial/\partial y_\xi$ in the rotor ellipsoidal coordinate system is obtained as:

$$\begin{aligned}\frac{\partial(\ )}{\partial y_\xi} = &\left(-\nu\sin\psi\cdot\frac{s_1}{s_2}\right)\frac{\partial(\ )}{\partial\nu} + \\ &+\left(\eta\sin\psi\cdot\frac{s_1}{s_2}\right)\frac{\partial(\ )}{\partial\eta} + \left(\frac{\cos\psi}{s_1}\right)\frac{\partial(\ )}{\partial\psi}\end{aligned} \tag{59}$$

and

$$\begin{aligned}\frac{\partial(\ )}{\partial z_\xi} = &\left(-\nu\sin\alpha\cos\psi\cdot\frac{s_1}{s_2}+\eta\cos\alpha\cdot\frac{1-\nu^2}{s_2}\right)\frac{\partial(\ )}{\partial\nu} + \\ &+\left(\eta\sin\alpha\cos\psi\cdot\frac{s_1}{s_2}+\nu\cos\alpha\cdot\frac{1+\eta^2}{s_2}\right)\frac{\partial(\ )}{\partial\eta} + \\ &+\left(-\frac{\sin\alpha\sin\psi}{s_1}\right)\frac{\partial(\ )}{\partial\psi}\end{aligned} \tag{60}$$

where $s_1 = \sqrt{(1-\nu^2)(1+\eta^2)}$ and $s_2 = \nu^2+\eta^2$.

Factorial expressions

In the following expressions the double factorial is used which is defined as:

$$\begin{aligned}&n!! = (n)(n-2)(n-4)\cdots(2) \quad for \quad n = even\\ &n!! = (n)(n-2)(n-4)\cdots(1) \quad for \quad n = odd\\ &and \quad 0!! = 1!! = 1\end{aligned} \tag{61}$$

Therewith:

$$H_n^m = \frac{(n+m-1)!!(n-m-1)!!}{(n+m)!!(n-m)!!} \tag{62}$$

and

$$\begin{aligned}\frac{\bar{P}_n^m(\nu)}{\nu} = &\sqrt{(2n+1)H_n^m}\cdot\\ &\cdot\sum_{q=m,m+2,..}^{n-1} r^q\,\frac{(-1)^{\frac{q-m}{2}}(n+q)!!}{(q-m)!!(q+m)!!(n-q-1)!!}\end{aligned} \tag{63}$$

In [15] analytical expressions for the gain matrices $\bar{\bar{L}}$ have been worked out:

$$\bar{\bar{L}}_{jn}^{0m\,c} = X^m\cdot\Gamma_{jn}^{0m} \tag{64}$$

$$\bar{\bar{L}}_{jn}^{rm\,c} = \left(X^{m-r}+(-1)^i\cdot X^{m+r}\right)\cdot\Gamma_{jn}^{rm} \tag{65}$$

$$\bar{\bar{L}}_{jn}^{rm\,s} = \left(X^{m-r}-(-1)^i\cdot X^{m+r}\right)\cdot\Gamma_{jn}^{rm} \tag{66}$$

with: $X = \tan|\chi/2|$ and $l = \min(r,m)$. The Γ function is defined as:

$$\Gamma_{jn}^{rm} = \frac{(-1)^{\frac{n+j-2r}{2}}\,4\sqrt{(2n+1)(2j+1)}}{\pi(j+n)(j+n+2)((j-n)^2-1)} \qquad r+m=even \tag{67}$$

$$\Gamma_{jn}^{rm} = \frac{sign(r-m)}{\sqrt{(2n+1)(2j+1)}} \qquad r+m=odd;\ j=n\pm1 \tag{68}$$

$$\Gamma_{jn}^{rm} = 0 \qquad r+m=odd;\ j\neq n\pm1 \tag{69}$$

Relation between harmonics and states

In general, for each harmonic *m* as many shape states as wanted can be taken into account. It seems reasonable, however, to limit the shape number *n* in relation to the maximum harmonic number used: $n_{max} = m_{max}+1$. This corresponds to a maximum order of radial shape function as used in (63) of $r^{m_{max}}$. Now the following relation between harmonics and states occurs:

m	0	1	2	3	4	5	6	7	8
states	1	3	6	10	15	21	28	36	45